Silicon Polygonal Microdisk Resonators

Chao Li, Linjie Zhou, Shengmei Zheng, and Andrew W. Poon, *Associate Member, IEEE*

(Invited Paper)

Abstract—We show silicon polygonal microdisk resonators with laterally coupled waveguides. Our two-dimensional (2-D) finite-difference time-domain (FDTD) simulations and spatial Fourier analysis reveal that waveguide coupling to a planar microstructure with a sufficiently long and flat coupling sidewall enables directional wave vector coupling in the microstructure. Similar analysis shows that waveguide coupling to a polygonal microresonator flat sidewall enables preferential coupling to only a few resonance modes in large-sized polygonal microresonators. Our experiments on silicon waveguide-coupled 50-μm octagonal microresonators demonstrate only two dominant modes, with a Q of about 10^4 and an extinction ratio (ER) of about 15 dB. We also demonstrate square and hexagonal silicon microresonators with nearly single dominant modes, a Q of the order of 10^3, and an ER exceeding 10 dB.

Index Terms—Hexagonal microresonators, microdisk, microresonators, octagonal microresonators, polygonal microdisk resonators, silicon photonics, square microresonators, waveguide-coupled.

I. INTRODUCTION

SILICON-BASED high-index-contrast optical microresonators that are of a high Q, are micrometer sized, and enable efficient input and output coupling with integrated waveguides on a chip have seen substantial advancements in the recent years. Most of these employ conventional circular and racetrack microring [1]–[10] and whispering-gallery (WG) microdisk resonators [11]–[13]. For instance, high-Q microring resonators in silicon-on-insulator (SOI) [1], [4]–[10] and silicon nitride-on-silica (SiN-on-SiO$_2$) [2], [3] have been demonstrated for optical networks and biochemical sensing applications. On the active device front, the silicon electrooptic microring modulators have reached gigahertz speeds [14]. Moreover, microelectromechanical-systems (MEMS)-enabled mechanically tunable microring and microdisk resonators [15], [16] have been demonstrated. However, circular microring and microdisk have undesirable micrometer-scale curved sidewalls that impose a limited interaction length and a tight submicrometer gap (~ 0.1–$0.2\ \mu$m) for lateral coupling with straight waveg-

uides. Besides, high-index-contrast waveguide-coupled WG microdisk resonators tend to be multimode.

As an alternative microresonator design, polygonal microdisk resonators in the shape of square [17]–[23], hexagon [24]–[26], and octagon [27], [28] have been proposed recently. Compared with conventional circular microring and microdisk resonators [1]–[5], [11]–[13], these polygonal microresonators have the key merit of possessing relatively long coupling lengths along the microresonator flat sidewalls for lateral coupling with straight waveguides. Compared with racetrack microring resonators [6]–[10], polygonal microdisk resonators eliminate the undesirable microring inner sidewall scattering loss, and enable multiple flat sidewalls for coupling to waveguide crossing architectures [22]. However, it has also been recognized that these polygonal microdisk resonators are intrinsically multimode [18]. Previously, we experimentally demonstrated silicon nitride octagonal [27], [28] and hexagonal microresonators [25], [26] as channel add–drop filters.

Here, we show silicon polygonal microdisk resonators with laterally coupled waveguides. Our two-dimensional (2-D) finite-difference time-domain (FDTD) simulations, and spatial Fourier analysis of the simulated field patterns, reveal that waveguide lateral coupling to planar microstructures with sufficiently long and flat sidewalls enables directional wave vectors in the coupled microstructures. Our simulations also suggest fewer coupled modes in waveguide-coupled polygonal microresonators than in waveguide-coupled circular microdisk resonators of the same cavity size and refractive index contrast. Our experiments demonstrate waveguide coupling to only two dominant modes for 50-μm octagonal microresonators, and nearly single modes for square and hexagonal microresonators of the same size in thin SOI substrates.

The paper is organized as follows. Section II reviews the essential ray and wave-optics concepts in the context of waveguide-coupled polygonal microresonators. Section III presents the analysis of waveguide-coupled planar microstructures with flat and curved coupling sidewalls. Section IV discusses the analysis of waveguide-coupled polygonal microresonators with emphasis on octagonal microresonators. Section V describes the device fabrication. Section VI presents the device measurements and analysis. Section VII discusses the design issues and presents conclusions.

C. Li, L. Zhou, and A. W. Poon are with the Department of Electronic and Computer Engineering, The Hong Kong University of Science and Technology, Hong Kong (e-mail: lichao@ust.hk; zhoulj@ust.hk; eeawpoon@ust.hk).

S. Zheng was with the Department of Electronic and Computer Engineering, The Hong Kong University of Science and Technology, Hong Kong. She is now with the Hong Kong Applied Science and Technology Research Institute Company Ltd., Hong Kong (e-mail: smzheng@astri.org).

II. RAY AND WAVE-OPTICS CONCEPTS

We begin with reviewing the essential ray and wave-optics concepts in the context of waveguide-coupled polygonal microcavities. Fig. 1 depicts the N-bounce ($N = 4, 6, 8$) ray orbits with incident angle θ in waveguide-coupled octagonal,
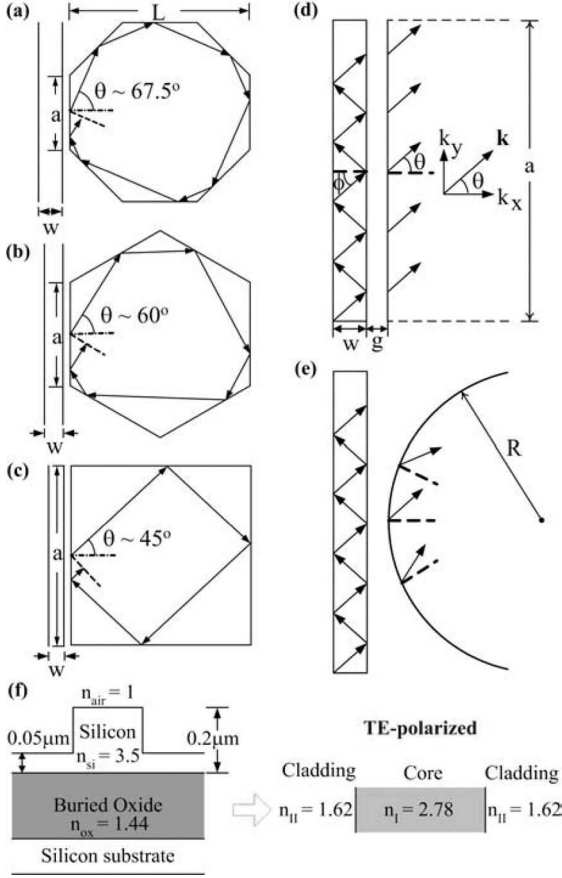
Fig. 1. (a)–(c) Schematics of waveguide-coupled polygonal microresonators and N-bounce ray orbits with incident angle θ. The round-trip matched wavefronts are shown (*dashed lines*). (a) Octagonal microresonator with an eight-bounce ray orbit. (b) Hexagonal microresonator with a six-bounce ray orbit. (c) Square microresonator with a four-bounce ray orbit. w: waveguide width. L: sidewall-to-sidewall distance. a: sidewall length. (d) and (e) Schematics of the waveguide-coupled flat sidewall of length a and the curved sidewall of radius R. The coupled $\boldsymbol{k}$-vectors along the entire flat sidewall are directional. The coupled $\boldsymbol{k}$-vectors along the curved sidewall exhibit an angular distribution. ϕ: waveguide mode angle. $\boldsymbol{k}$: coupled $\boldsymbol{k}$-vector. θ: $\boldsymbol{k}$ angle relative to the sidewall normal. g: air-gap spacing. (f) Cross section of the rib waveguide and the effective 2-D structure for the TE polarization.

hexagonal, and square microcavities. It has been recognized that both closed- and open-loop N-bounce ray orbits of different round-trip path lengths in polygonal cavities can be wavefront-matched with the input-coupled rays upon each round trip, thereby supporting multiple modes [18]. The dashed lines shown in Fig. 1 represent typical round-trip matched wavefronts. We denote the cavity sidewall-to-sidewall distance as L. The sidewall lengths a are given as $(\sqrt{2}-1)L$ for octagonal cavities, as $(\sqrt{3}/3)L$ for hexagonal cavities, and as L for square cavities. It should be emphasized that octagonal cavities also support four-bounce wavefront-matched ray orbits. The eight-, six-, and four-bounce wavefront-matched round-trip path lengths are given as follows [18], [25], [27]:

$$
\begin{aligned}
l(\theta) &= 4(\sqrt{2}-1)L[\sin\theta + \cos(\theta - 45°)] && \text{eight-bounce} \\
l(\theta) &= 3L\sin(\theta + 30°) && \text{six-bounce} \\
l(\theta) &= 2L(\cos\theta + \sin\theta) && \text{four-bounce.}
\end{aligned}
\tag{1}
$$

We remark that $l(\theta)$ is independent of the ray input-coupling position along the polygonal cavity flat sidewall. The free spectral range (FSR) for the N-bounce modes is then approximately given as $\lambda_0^2/nl(\theta)$, where λ_0 is the free-space resonance wavelength, and n is the microdisk cavity refractive index.

The incident angle θ needs to satisfy $\theta_c < \theta < [((N-2)180°/N) - \theta_c] - \theta_c$, where θ_c is the total internal reflection (TIR) critical angle in order to partially confine the N-bounce trajectories by TIR. This angle range is relatively large for silicon. However, ray tracing suggests much stringent θ ranges in order to ensure at least one round trip: $64.1° < \theta < 70.2°$ for an octagonal-cavity eight-bounce orbit, $38.4° < \theta < 50.4°$ for an octagonal-cavity four-bounce orbit, $53.4° < \theta < 64.7°$ for a hexagonal-cavity six-bounce orbit, and $26.5° < \theta < 56.3°$ for a square-cavity four-bounce orbit. By choosing particular values of θ, we can in principle selectively couple to N-bounce ray orbits in polygonal cavities [26], [27]. In case of waveguide coupling, we can choose θ by properly designing the waveguide width under a fixed refractive index and vertical waveguide profile [26]. We remark that eight- and four-bounce ray orbits in octagonal cavities and four-bounce ray orbits in square cavities always enable symmetric input and output coupling to the cavity parallel sidewalls.

III. ANALYSIS OF WAVEGUIDE COUPLING TO PLANAR MICROSTRUCTURES

Here, we numerically simulate the waveguide coupling to planar microstructures with flat and curved coupling sidewalls. When a single-mode waveguide is evanescently input-coupled to a planar microstructure of the same refractive index and with a flat coupling sidewall that is sufficiently long, it is intuitive that the coupled wave vectors are directed in angles θ (relative to the flat sidewall normal) centered about the waveguide mode wave vector angle ϕ (relative to the waveguide sidewall normal). In contrast, the coupled wave vectors along a relatively short arc length of a curved sidewall can exhibit a relatively large angular distribution. Fig. 1(d) and (e) shows schematically the wave vectors in waveguide-coupled planar microstructures with flat and curved coupling sidewalls.

We employ commercial FDTD numerical simulations tool [29]. We adopt semi-infinite planar microstructures with only single sidewalls for coupling and perfectly matched layers (PML) on the three other sides. We consider 2-D design and analysis, with effective refractive index to account for the vertical dimension. Specifically, we calculate the effective refractive index for the TE-polarization (electric field parallel to the chip) for the 0.2-μm-thick silicon waveguide core (~ 2.78) and for the 0.05-μm-thick silicon slab layer (~ 1.62), assuming an air upper cladding and a silica lower cladding. Fig. 1(f) illustrates the rib waveguide cross section and the effective 2-D structure.

Fig. 2(a) and (b) shows the representative FDTD-simulated steady-state $\boldsymbol{H}$-field patterns (TE-polarization) for silicon waveguide-coupled planar microstructures with a flat sidewall ($a = 10\,\mu$m) and a curved sidewall (radius of curvature of 5 μm). We choose the waveguide width $w = 0.3\,\mu$m and the air-gap
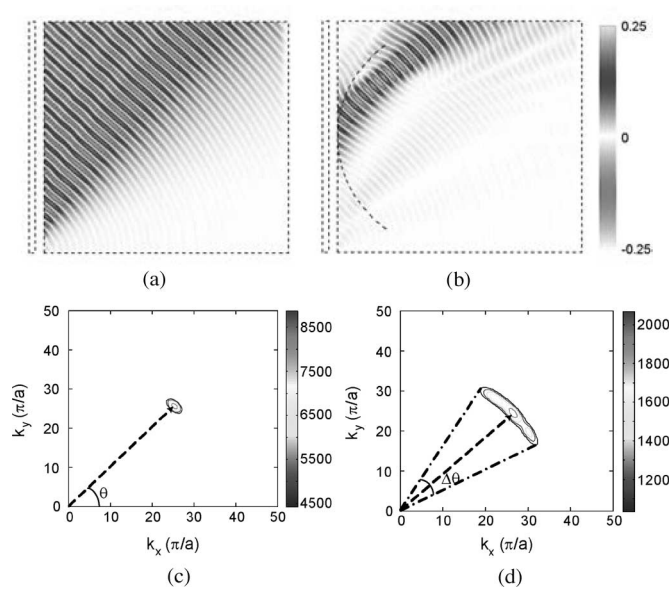
Fig. 2.   FDTD-simulated TE-polarized steady-state $\boldsymbol{H}$-field patterns for the silicon waveguide-coupled planar microstructures. (a) Flat sidewall of length $a = 10$ μm. (b) Curved sidewall (radius of curvature of 5 μm). The area of size a under Fourier analysis is shown (*dashed-line box*). (c) and (d) Fourier analysis of the simulated steady-state field patterns. The contours represent the $\boldsymbol{k}$-vectors spanning within half-maximum of the angular distributions. The coupled $\boldsymbol{k}$-vectors central angles θ (*dashed arrows*) and the k-space angular distribution $\Delta\theta$ (*dashed line*) are shown.

spacing $g = 0.35$ μm. Only the coupled fields in the planar microstructures are shown. Our simulations suggest that waveguide coupling to the flat sidewall occurs along the entire flat sidewall and the coupled wavefronts are nearly flat; whereas, waveguide coupling to the curved sidewall occurs only along a relatively short arc length and the coupled wavefronts exhibit a considerable angular distribution.

In detail, we apply in the simulations a submicrometer slab waveguide fundamental mode profile in the lateral direction. We adopt a 20-nm spatial grid size and a 0.04-fs temporal step. A PML of reflectivity 10^{-8} and a thickness of 0.5 μm in both x- and y-directions is applied at the simulation window boundaries. Steady-state field patterns are then obtained by launching a continuous-wave at particular wavelengths (1550 nm).

We analyze the simulated field patterns in $\boldsymbol{k}$-space by means of spatial Fourier transform. Fig. 2(c) and (d) shows the spatial Fourier analysis of the simulated field patterns in the planar microstructures with flat and curved coupling sidewall. The dashed square boxes with size a in Fig. 2(a) and (b) show the real-space area under Fourier analysis. In each case, we use $a = 10$ μm. We define the wave vector components k_x and k_y, in units of π/a, and $k_x^2 + k_y^2 = (nk)^2$, where n is the effective refractive index (2.78) and k is the free-space wave vector. We observe that the coupled $\boldsymbol{k}$-vector angles are only well defined in case the arc lengths are sufficiently long or the sidewall is flat. We note that the $\boldsymbol{k}$-space contour plots only span full-width-half-maximum distributions in order to highlight the major $\boldsymbol{k}$-vector angular components.
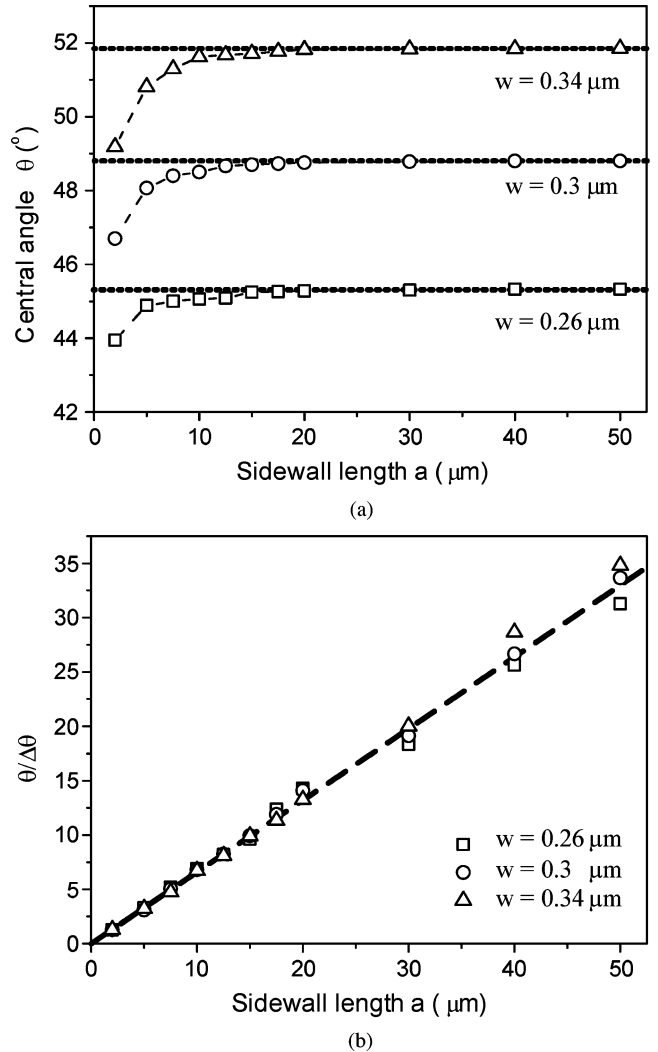

Fig. 3.   Simulated (a) θs and (b) $\theta/\Delta\theta$s of the waveguide-coupled planar microstructures with various sidewall lengths and different waveguide widths. Visual aid has been provided (*dashed lines*).

The coupled $\boldsymbol{k}$-vectors become directional only with sufficiently long and flat coupling sidewalls. We observe that the $\boldsymbol{k}$-vector angular distributions are sharpened (both narrowed in angular widths and enhanced in peak heights) with the sidewall length. We also see that θ has an overall increase up to some saturating values as the sidewall is lengthened. Here, the $\boldsymbol{k}$-vectors' angular distribution is given as $\theta/\Delta\theta$. Fig. 3(a) and (b) shows the values of simulated θ and $\theta/\Delta\theta$ at various sidewall lengths of different waveguide widths w. For each w, θ rises sharply with increases in a from 2 to 5 μm, and saturates at a certain value when a exceeds about 7.5 μm. We observe that the saturated θs in the waveguide-coupled planar microstructures match well with the analytically calculated ϕs for the waveguide modes. The dashed lines indicate the analytically calculated waveguide mode angles ϕs. Interestingly, $\theta/\Delta\theta$ linearly rises from ~ 2 to ~ 32 when a lengthens from ~ 2 to ~ 50 μm, and exhibit the same slope for the different waveguide widths.
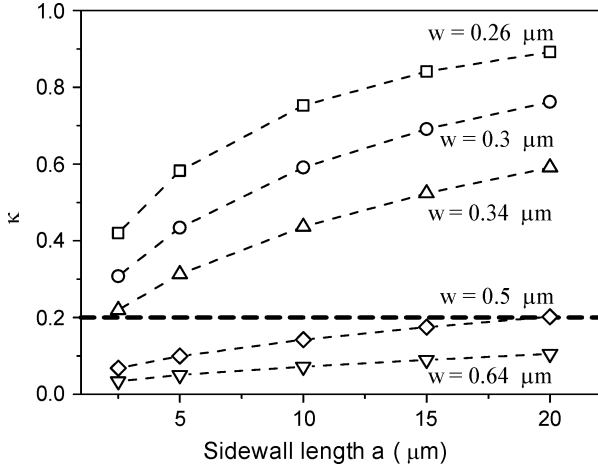
Fig. 4. Simulated coupling coefficient κ for waveguide coupling to planar microstructures as a function of sidewall length with various waveguide widths. Visual aid has been provided (*dashed lines*).

Here, we examine the waveguide microstructure field amplitude coupling coefficient κ under various configurations. We obtain κ from our simulations as the ratio of the total field amplitude detected along the dashed-line square entire upper and right boundary [Fig. 2(a) and (b)] to the input-coupled field amplitude at the waveguide. Fig. 4 shows the simulated κ using flat sidewalls of various values of a of different waveguide widths. As expected, κ rises with a. Yet, κ drops with w. The simulated κ values are relatively low (below ~ 0.2) for $w \geq 0.5\,\mu m$ (with a relatively wide coupling gap $g = 0.35\,\mu m$). We see that κ drops below 0.1 as w exceeds 0.64 μm (where $\phi \sim 67.5°$ is desirable for eight-bounce modes in octagonal microresonators) for $g = 0.35\,\mu m$.

In summary, our numerical analysis on silicon waveguide-coupled planar microstructures suggests that in order to obtain a reasonable κ, say above 0.2 (an arbitrary reference), we only consider w to be below 0.5 μm. We see that only four- and six-bounce ray orbits can be effectively coupled (Figs. 3 and 4). Hence, for directional coupling to four-bounce ray orbits in octagonal and square microcavities, we can apply $w \sim 0.3\,\mu m$, with $g \sim 0.35\,\mu m$ for a as short as $\sim 5\,\mu m$.

IV. ANALYSIS OF WAVEGUIDE-COUPLED POLYGONAL MICRORESONATORS

Here, we study silicon waveguide-coupled polygonal microresonators using 2-D FDTD simulations, with emphasis on octagonal microresonators. We adopt the channel add-drop filter configuration of which the waveguides are input and output coupled to the microresonator parallel flat sidewalls. We examine: 1) the effect of coupling sidewall length on mode k-vectors; 2) the cavity shape dependence; 3) the cavity loss and the waveguide coupling coefficients based on Fabry–Perot model; 4) the roles of the rounded corners; and 5) the mode density estimation.

It should be first emphasized that the sharp corners of polygonal microresonators are long recognized as a major drawback for polygonal microresonators acting as high-Q resonant devices [21], [26], [27]. The surface wave propagating along flat sidewalls cannot follow the sharp transitions at cavity corners, resulting in excessive diffractive loss. In order to mitigate such drawback, we previously demonstrated tailoring the polygonal microresonator shapes with rounded corners at the photomask layout [28], [30]. We apply an arc with a radius of curvature R to each of the polygonal cavity corners. We then define the round-cornered polygonal microcavity shapes in terms of the relative radius R/L, where $R/L = 0$ means a sharp-cornered polygonal microresonator and $R/L = 0.5$ means a circular microdisk. In the case of octagonal microresonators, the flat sidewall length $a = (\sqrt{2} - 1)(L - 2R)$. However, we caution that the coupling does not only occur along the flat sidewall length region but also include a small portion of the round-corner arc lengths.

A. Effect of Coupling Sidewall Length on Mode k-Vectors

Fig. 5(a) shows the FDTD-simulated throughput-port spectra (TE polarization) of waveguide-coupled round-cornered $(R/L = 0.3)$ octagonal microresonator filters with coupling length $a = 7.6\,\mu m$ ($L = 30\,\mu m$) and $a = 5.5\,\mu m$ ($L = 20\,\mu m$). We use $w = 0.3\,\mu m$ and $g = 0.35\,\mu m$. The value of w is chosen as 0.3 μm in order to preferentially couple to four-bounce ray orbits. We observe only two dominant modes (denoted as A and B) with the longer coupling length, while we see about five modes with the shorter coupling length. Based on the planar microstructure analysis (see Section III, Fig. 3), we see that θs are $\sim 48.1°$ with $a \sim 5.5\,\mu m$ and $\sim 48.4°$ with $a \sim 7.6\,\mu m$, while $\Delta\theta$s are $\sim 13.4°$ and $\sim 9.0°$, respectively. Thus, the longer the sidewall coupling length, the fewer are the coupled resonance modes.

Fig. 5(b) and (c) shows the simulated steady-state $\boldsymbol{H}$-field patterns at resonances A and B. At resonance A, the mode-field pattern clearly displays wavefronts propagating in near-45° four-bounce ray orbits. At resonance B, the mode-field pattern suggests two interfering four-bounce ray orbits.

Fig. 5(d) and (e) shows the Fourier analysis of the mode-field patterns. The $\boldsymbol{k}$-space profile suggests a maximum around $\theta = 45°$ ($k_x \sim k_y$) for resonance A, whereas, resonance B displays two maxima of nearly equal amplitudes around $\theta_1 = 49.4°$ and $\theta_2 = 40.6°$. The angle difference between modes A and B is $\sim 4.4°$, which is within the coupled k-vector angular span $\Delta\theta$ of $\sim 9.0°$, based on our analysis of waveguide-coupled planar microstructures (Fig. 3).

B. Cavity Shape Dependence

We also study the mode characteristics as a function of cavity shapes of the waveguide-coupled octagonal microresonators. Fig. 6(a)–(d) shows the FDTD-simulated throughput-port spectra (TE polarization) of the waveguide-coupled octagonal microresonator filters with representative R/L ratios of 0, 0.1, 0.4, and 0.5. We choose $L = 30\,\mu m$, $w = 0.3\,\mu m$, and $g = 0.35\,\mu m$. The spectra display about two to three modes except for $R/L = 0.5$ (circular microdisk), which displays about five modes. For each R/L, we choose the mode with the maximum extinction ratio (ER) (labeled with an asterisk) within the spectral range of interest, for further analysis.

(a)

Fig. 6.   Simulated TE-polarized throughput spectra of waveguide-coupled round-cornered octagonal microresonators with various R/L values. (a) 0. (b) 0.1. (c) 0.4. (d) 0.5. The modes marked by asterisk represent the maximum ER peaks for each R/L.

(b)   (d)

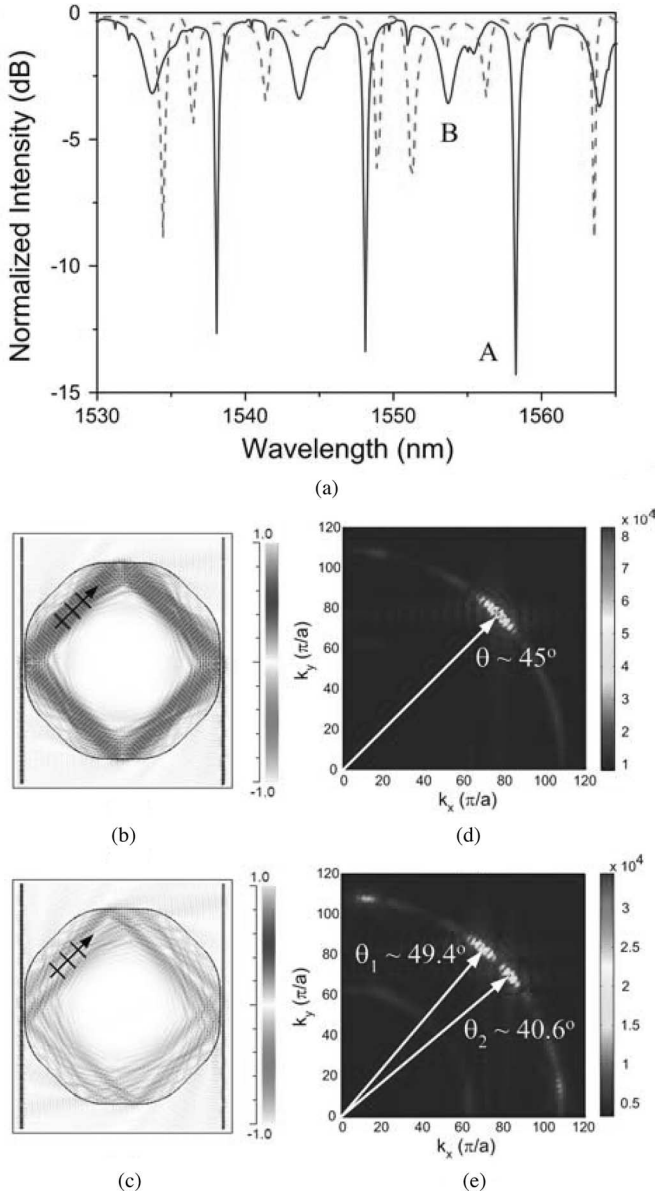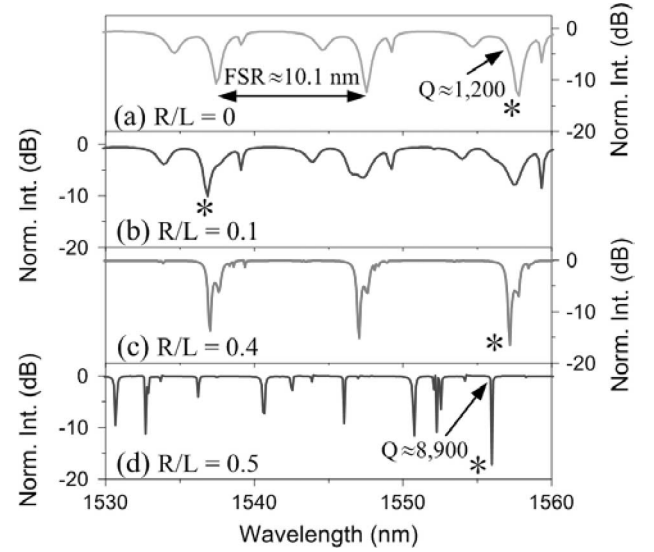(c)   (e)

Fig. 5.   (a) FDTD-simulated throughput-port spectra (TE polarization) of waveguide-coupled round-cornered octagonal microresonator filters ($R/L = 0.3$) with coupling length $a \sim 7.6~\mu$m (*solid line*) and $a \sim 5.5~\mu$m (*dashed line*). (b) and (c) Simulated steady-state H-field patterns of the waveguide-coupled round-cornered ($R/L = 0.3$) octagonal microresonators at resonances A and B. $L = 30~\mu$m. $w = 0.3~\mu$m. $g = 0.35~\mu$m. (d) and (e) Fourier analysis of the mode-field patterns. The dominant angles of the coupled $\boldsymbol{k}$-vectors are shown (*arrows*).

The simulated spectra of the octagonal microresonators ($R/L = 0 - 0.4$) exhibit an FSR of about 10.1 nm. The simulated FSR is consistent with the calculated FSR of about 10.2 nm, assuming four-bounce ray orbits $\theta \sim 48.4°$ given by $w = 0.3~\mu$m and using (1) with effective refractive index $n = 2.78$. The FSR of the control circular microdisk is about 10.0 nm, which also suggests high-radial-order WG modes propagating in four-bounce ray orbits.

Fig. 7(a) shows the simulated ER and Q at various R/L ratios based on the mode denoted by an asterisk. Both ER and

Q generally rise with R/L ratio. At $R/L = 0.1$, both ER and Q display a local minimum.

C. Fabry–Perot-Based Analysis: Cavity Loss and Waveguide Coupling Coefficients

Here, we interpret the simulated spectra of the waveguide-coupled octagonal microresonators by means of a scalar-field Fabry–Perot-like model [31]. We approximately extract from the simulated spectra the round-trip cavity loss $A = \exp(\alpha l)$, where α is the cavity loss field coefficient, and the waveguide–microresonator coupling field coefficient κ at various R/L ratios (or sidewall lengths). The model assumes single-mode resonances. Furthermore, the model assumes lossless symmetric input and output coupling between the waveguides and the microresonator, while the microresonator is assumed to be lossy. From the simulated resonance ERs and the Q values, we solve for A and κ using the following equations:

$$
\begin{aligned}
\mathrm{ER\,(dB)} &= -10 \log(I_{\mathrm{tr}}/I_{\mathrm{t\,max}}) \\
&= -10 \log \left\{ 1 - \frac{4A|\kappa|^2[1 - A^2(1 - |\kappa|^2)]}{(1 + A)^2[1 - A(1 - |\kappa|^2)]^2} \right\} \quad (2)
\end{aligned}
$$

$$
\begin{aligned}
Q &= \frac{\lambda_0}{\Delta \lambda} \\
&= \frac{\lambda_0 \pi}{\mathrm{FSR}} \left[2 \sin^{-1} \left(\sqrt{\frac{[1 - A(1 - |\kappa|^2)]^2}{2(1 + A^2(1 - |\kappa|^2)^2)}} \right) \right]^{-1} \quad (3)
\end{aligned}
$$

where $I_{\mathrm{t\,max}}$ is the throughput maximum intensity, I_{tr} is the throughput intensity at resonance wavelengths, and $\Delta \lambda$ is the resonance linewidth.

Fig. 7(b) shows the model-extracted κ (circles) and A (squares) at various R/L ratios for $L = 30~\mu$m, based on the simulated ER and Q values [Fig. 7(a)]. The κ values drop
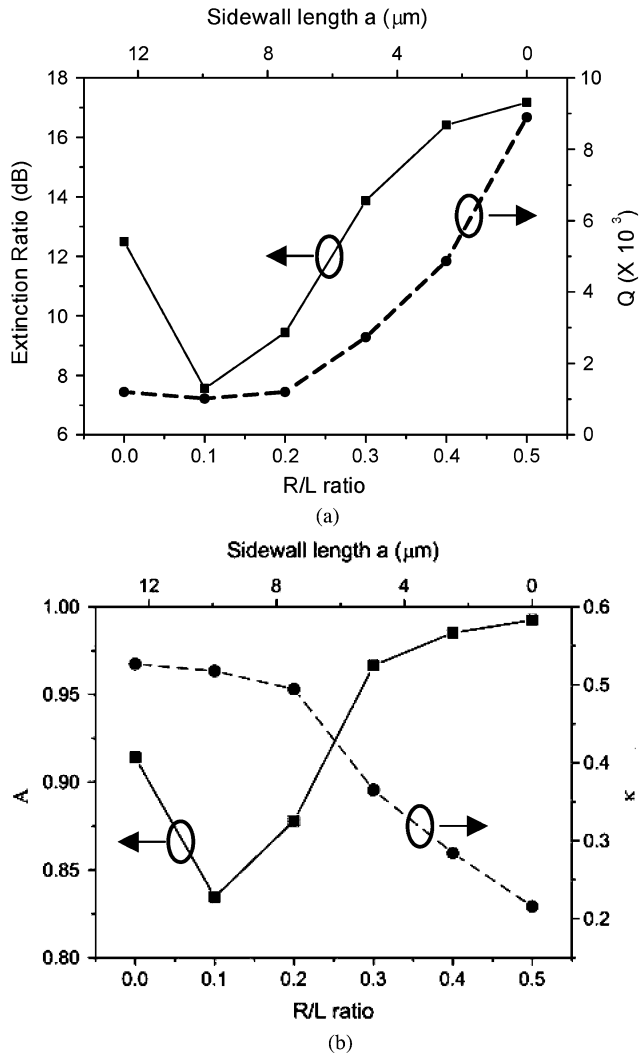
Fig. 7. (a) Simulated ER (*squares*) and Q (*circles*) at various R/L ratios. (b) Model-extracted round-trip cavity loss A (*squares*) and coupling field coefficient κ (*circles*) at various R/L ratios. Visual aid has been provided (*lines*).
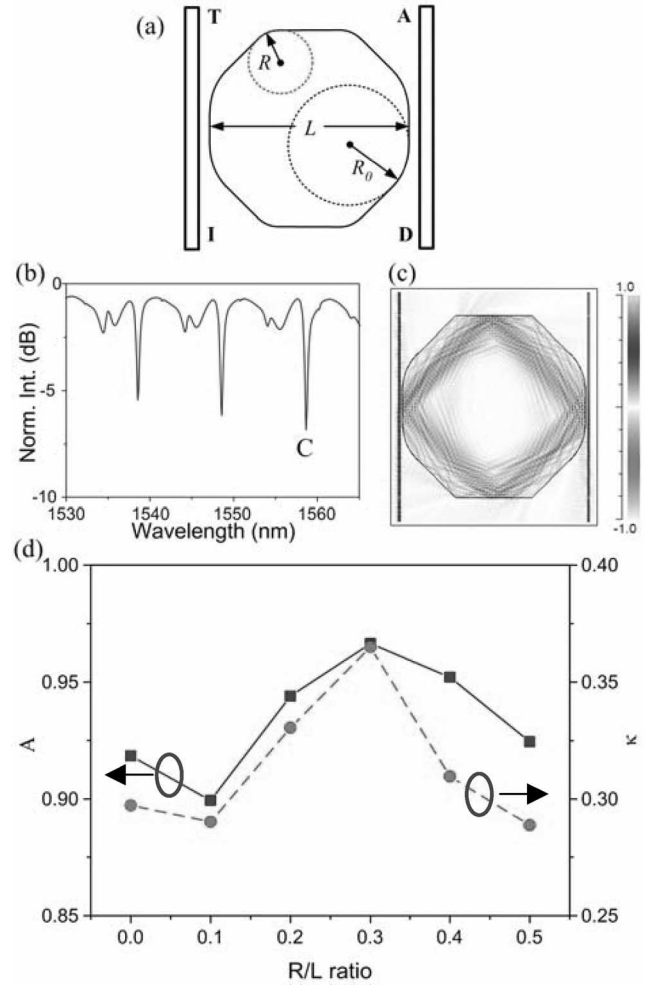

Fig. 8. (a) Schematic of the waveguide-coupled octagonal microresonator channel add-drop filter with selectively rounded corners. I: input. T: throughput. D: drop. A: add. (b) Simulated throughput-port spectrum (TE polarization) of a 30-μm waveguide-coupled octagonal microresonator with four sharp corners. $R_0/L = 0.3$. (c) Simulated steady-state $\boldsymbol{H}$-field patterns of mode C. (d) Model-extracted A (*squares*) and κ (*circles*) at various R/L ratios. Visual aid has been provided (*lines*).

with the R/L ratio (reducing sidewall length) as expected. We observe a qualitative agreement between the extracted κ values and the simulated ones in the waveguide-coupled planar microstructures analysis of the same L and w (Fig. 4). The extracted A qualitatively follows the simulated ER trend and dips at $R/L = 0.1$, suggesting an enhanced cavity loss. However, we caution that the simulated spectrum at $R/L = 0.1$ [Fig. 6(b)] suggests inhomogeneous broadening with at least two similarly coupled modes, and thus, the single-mode Fabry–Perot model may not be totally applicable. As R/L exceeds about 0.1, the extracted A rises (reduced cavity loss) and approaches unity (essentially zero cavity loss) as the microresonator shape becomes circular.

D. Effects of the Rounded Corners

The effects of the rounded corners not only reduce the surface wave leakage but also change the waveguide–microresonator coupling condition. In order to examine the effects of the

rounded corners in octagonal microresonators, we only vary the radii of the four corners away from the two coupling regions while keeping the four rounded corners adjacent to the waveguides in the same shape ($R/L = 0.3$), as depicted in Fig. 8(a). Thus, we fix the waveguide–microresonator coupling interface.

Fig. 8(b) shows the simulated throughput-port spectrum (TE polarization) of a 30-μm octagonal microresonator with four sharp corners ($R/L = 0$). We observe less ER compared with the round-cornered microresonator of the shape $R/L = 0.3$ [Fig. 5(a), solid-line spectrum]. Mode C exhibits a $Q \sim 3000$ and an ER of 6.2 dB, while the round-cornered octagonal microdisk mode A [Fig. 5(a)] displays a $Q \sim 2700$ and an ER of 13.9 dB. We analyze the model-extracted κ and A for modes C and A. For mode C, the extracted $\kappa = 0.30$ and the extracted $A = 0.92$, whereas, for mode A, the extracted $\kappa = 0.36$ and the extracted $A = 0.97$. We see that the four sharp corners impose a reduced waveguide coupling and an enhanced cavity loss to the octagonal microresonator. Fig. 8(c) shows the simulated

steady-state $\boldsymbol{H}$-field pattern for mode C. We attribute the relatively weak internal-field amplitudes for mode C [compared with mode A in Fig. 5(b)] to the excess diffractive loss at the four sharp corners.

Fig. 8(d) shows the model-extracted A and κ at various R/L ratios of the four corners away from the waveguide coupling regions. Interestingly, we observe similar trends for the extracted A and κ, with both A and κ displaying a local minimum at $R/L = 0.1$ and a local maximum at $R/L = 0.3$. We reason that by tailoring the rounded corners of the cavity, the modified cavity boundary condition then affects the waveguide–microresonator coupling.

E. Mode Density Estimation

Here, we seek to approximately extract the microresonator mode densities under the various microresonator shapes based on the simulated spectra. We heuristically define the mode density as $M = N_{\mathrm{m}}/(\Delta|k| \cdot |k| \cdot \Delta\theta)$, where N_m is the number of modes, $\Delta|k| = 2\pi/l$ (l is the wavefront-matched round-trip path length), and $|k| = n2\pi/\lambda_0$ (n is the effective index). Thus, we express M as follows:

$$M = \frac{N_{\mathrm{m}}l\lambda_0}{n(4\pi^2)\Delta\theta}. \tag{4}$$

M is quadratically dependent on the microresonator size L, because both l and $1/\Delta\theta$ are linearly dependent on L. In order to approximately extract M, we first obtain $\Delta\theta$ from the planar microstructure analysis using various shapes (Fig. 3). For $L = 30$ μm, $\Delta\theta \sim 5.9°$ for the sharp-cornered octagonal microresonator, and $\Delta\theta \sim 9.0°$ for the round-cornered octagonal microresonators with an R/L of 0.3. The circular microdisk exhibits much larger $\Delta\theta \sim 22.2°$. We obtain l based on the FSR, and λ_0 according to the simulated spectra. By counting the number of distinct mode order in the spectra, we can then estimate M. For the sharp-cornered octagonal microresonator, we estimate $M \sim 35.7$ modes $\cdot\mu$m^2 using $N_{\mathrm{m}} = 3$ [Fig. 6(a)]. For the round-cornered octagonal microresonator with $R/L = 0.3$, we estimate $M \sim 15.5$ modes $\cdot\mu$m^2 using $N_{\mathrm{m}} = 2$ [Fig. 5(a)]. For the circular microdisk, we estimate $M \sim 16.1$ modes $\cdot\mu$m^2 using $N_{\mathrm{m}} = 5$ [Fig. 6(d)]. Thus, in principle we can separately vary the mode density and the angular span of the coupled $\boldsymbol{k}$-vectors for attaining desirable single-mode characteristics. However, we caution that this estimation approach based on mode counting tends to have less accuracy when N_{m} is small.

V. DEVICE FABRICATIONS

We employ standard silicon nanofabrication processes. The device layout is defined by i-line photolithography, and transferred onto the device layer by CHF$_3$-based plasma etching. We use commercial SOI wafers [32] with a 0.2-μm-thick device layer on a 3-μm-thick buried-oxide layer. The deeply etch submicrometer waveguides and microresonators have a slab height of 0.05 μm. The chips are manually cleaved, and the end faces for fiber end-firing are unpolished.

Fig. 9(a) shows the top-view SEM of the fabricated silicon waveguide-coupled round-cornered octagonal microresonator
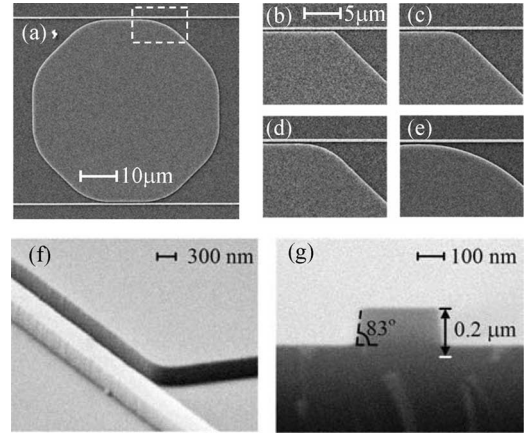

Fig. 9. (a) Top-view SEM of our fabricated silicon waveguide-coupled round-cornered octagonal microresonators with $R/L = 0.3$. $L = 50$ μm. $R = 15$ μm. $w = 0.34$ μm. $g = 0.36$ μm. (b)–(e) Zoom-in SEMs of the corner region with radius of 0, 5, 10, and 25 μm (*circular disk*). (f) Side-view SEM of the fabricated waveguide side-coupled with a flat sidewall. (g) Cross-sectional view SEM of the fabricated waveguide. The SOI device layer is 0.2-μm thick.

of $R/L = 0.3$ and $L = 50$ μm. The fabricated waveguide width w is $\sim$0.34 μm and the fabricated air-gap spacing g is $\sim$0.36 μm. Fig. 9(b)–(e) shows the zoom-in view SEMs of the microdisk corner regions with radii of 0, 5, 10, and 25 μm (circular disk). Fig. 9(f) shows the SEM of our fabricated waveguide coupled to a planar microstructure with a flat sidewall. The sidewall surfaces suggest reasonable roughness. Fig. 9(g) shows the cross-sectional view SEM of our fabricated waveguides. The waveguide sidewall slope angle is $\sim$83°.

VI. DEVICE MEASUREMENTS

A wavelength-tunable external-cavity diode laser (1510–1580-nm wavelength, linewidth $\approx$ 300 kHz) was end-fired to the waveguide input port using a tapered-lensed polarization-maintaining single-mode fiber (with a spot diameter of 2.5 μm). We imaged the throughput- and drop-port intensities using an objective lens (NA = 0.4) separately onto a multimode fiber after a TM/TE analyzer, and then lock-in detected by a photodiode detector. A near-IR camera was employed to image the throughput- and drop-port waveguides output intensities. The spectral resolution reported here is 0.02 nm limited by the wavelength tuning steps. The spectra are normalized with the transmitted intensity from the tapered-lensed fiber end-firing at the input-port waveguide.

We caution that our SOI waveguide loss is relatively high. The estimated waveguide propagation loss according to the cut-back method is $\sim$10–15 dB/cm. We attribute the high waveguide propagation loss to the substrate leakage loss [7] and the sidewall surface roughness that is partially limited by our photolithography and dry etching fabrication process.

Fig. 10(a)–(e) shows the measured TE-polarized throughput-port spectra of the silicon round-cornered octagonal microdisks with R/L ratios spanning from 0 to 0.3, and $R/L = 0.5$ used as a control. We observe only two distinct modes for the octagonal microresonators (except for $R/L = 0.1$), whereas we find the
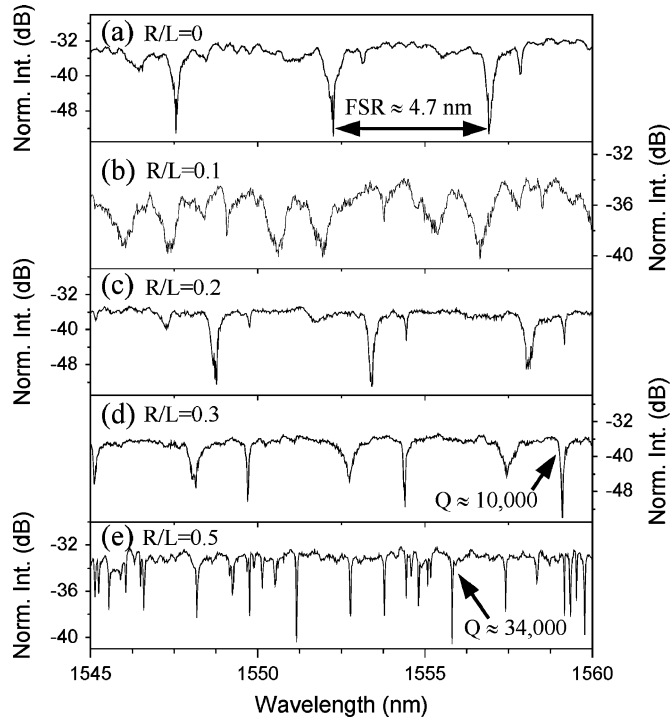
Fig. 10. Measured TE-polarized throughput spectra of the silicon round-cornered octagonal microdisks with various R/L values. (a) 0. (b) 0.1. (c) 0.2. (d) 0.3. (e) 0.5 (*circular microdisk*).
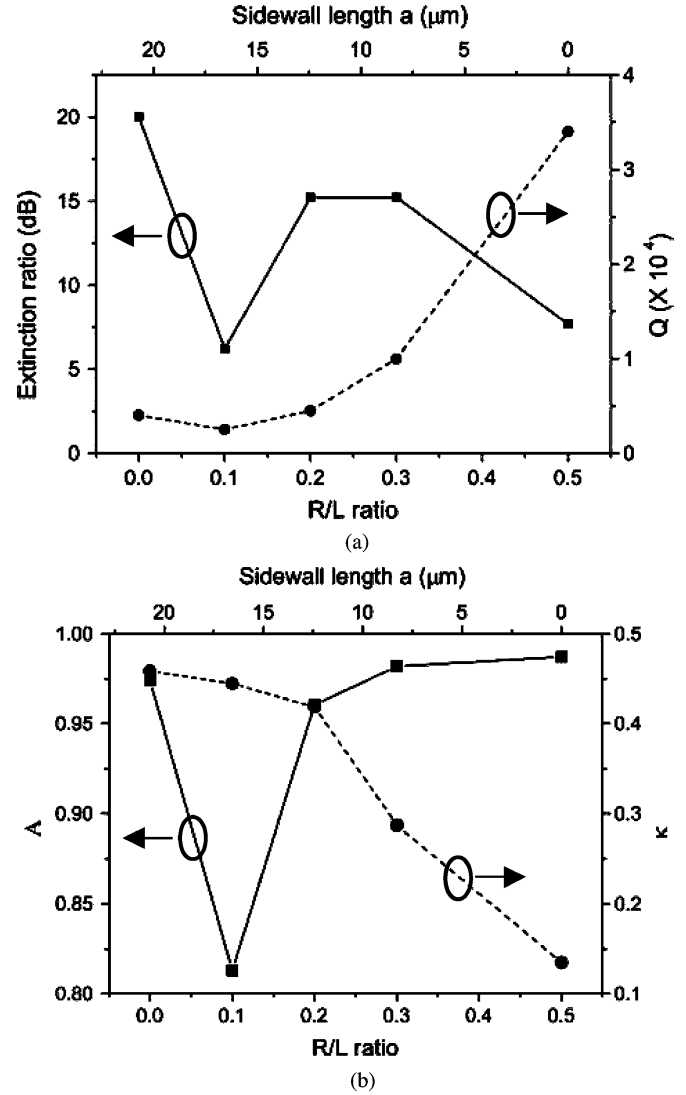

Fig. 11. (a) Measured ER (*squares*) and Q (*circles*) at various R/L ratios. (b) Model-extracted round-trip cavity loss A (*squares*) and coupling coefficient κ (*circles*) at various R/L ratios. Visual aid has been provided (*lines*).

circular microdisk displays to be highly multimode (about seven to eight). The measured FSR of the octagonal microresonators ($R/L = 0\text{--}0.3$) is about 4.7 nm, which is consistent with the calculated FSR of about 4.9 nm by assuming four-bounce ray orbits. The measured FSR of the circular microdisk is about 4.6 nm. For the octagonal microdisk, we obtain a maximum $Q \sim 10^4$ and an ER of ~ 15 dB with $R/L = 0.3$. With $R/L = 0.1$, we observe much broadened modes with Q and ER dropping to ~ 2500 and 6.2 dB, respectively. The circular microdisk spectrum displays high-Q ($\sim 3 \times 10^4$) resonances, yet with a maximum ER of only 7.7 dB.

Fig. 11(a) shows the measured ERs and Qs of the silicon octagonal microresonators at various R/L ratios. The Q rises nonlinearly with R/L ratio, which is consistent with the FDTD simulations [Fig. 7(a)]. The ER drops considerably near $R/L = 0.1$, also consistent with the simulated trend [Fig. 7(a)]. However, we see that the measured ER trend does not agree with that of the simulated trend of $L = 30$ μm when R/L exceeds about 0.3.

Fig. 11(b) shows the model-extracted κ and A at various R/L ratios based on the measured ERs and Q s [Fig. 11(a)]. The κ values drop with R/L ratio. We find that A dips at $R/L = 0.1$ and then approaches unity as the microresonator approaches a circular shape. Both the extracted κ and A display trends that are in qualitative agreement with those based on the FDTD simulations of $L = 30$-μm microresonator [Fig. 7(b)].

We attribute the two dominant modes observed in octagonal microresonators to the directional $\boldsymbol{k}$-vector coupling. The sidewall length for the sharp-cornered ($R/L = 0$) octagonal mi-

croresonator is about 20.7 μm. Such long sidewall lengths give well-defined $\boldsymbol{k}$-vectors at $\theta \sim 51.8°$ and $\Delta\theta \sim 3.7°$ (see Fig. 3). For round-cornered octagonal microresonators with R/L of 0.3 (coupling length of ~ 12 μm), $\Delta\theta$ is $\sim 6.4°$. Much larger $\Delta\theta \sim 18.4°$ is obtained for circular microdisk.

Based on the estimated mode densities M with $L = 30$-μm microresonator simulations, we deduce the 50-μm cavities mode densities M as ~ 99.2 modes·μm^2 for sharp-cornered octagonal microcavity, ~ 43.1 modes·μm^2 for round-cornered octagonal microcavity ($R/L = 0.3$), and ~ 44.7 modes·μm^2 for circular microdisk. Using (4), we estimate the number of modes $N_m \sim 3$ for a sharp-cornered octagonal microresonator, ~ 2 for a round-cornered octagonal microresonator ($R/L = 0.3$), and ~ 8 for a circular disk. The estimated number of modes is consistent with those observed in the measured spectra.

We remark that although our analysis can largely interpret why octagonal microresonators have fewer coupled modes, the

observed reduction in the ER at a particular round-cornered shape ($R/L = 0.1$) cannot be satisfactorily explained, and hence, should call for additional mechanisms. For example, multimode interference could occur as multiple orbits are coherently coupled along various locations of the microresonator flat sidewalls [26].

VII. DISCUSSION AND CONCLUSION

Our analysis and experiment show that silicon waveguide-coupled polygonal microresonators stand as viable alternative microresonator-based device structures for photonic integrated circuits. Here, we discuss some design rules and limitations.

In order to couple to even fewer and possibly single modes with four-bounce ray orbits, we should choose the coupled k-vector central angle even closer to $45°$ and also narrow the k-vector angular distribution. Fig. 12(a) shows the FDTD-simulated throughput-port spectrum (TE polarization) of a 25-μm waveguide-coupled square microresonator. Here, $w = 0.26\ \mu$m results in coupled k-vector central angle of $\sim 45.3°$. With 25-μm coupling sidewall length, $\Delta\theta$ is $\sim 2.8°$. We observe only single distinct mode. Fig. 12(b) shows the simulated steady-state H-field patterns at resonance "*." The mode field distributes in the whole square microresonator, but still displays four-bounce ray orbits.

Fig. 12(c) shows the measured TE-polarized throughput spectrum of a 50-μm silicon waveguide-coupled square microresonator. Inset shows the top-view SEM of the fabricated device. The fabricated waveguide width w is $\sim 0.3\ \mu$m and the fabricated air-gap spacing g is $\sim 0.45\ \mu$m. The spectrum displays only single modes with a $Q \sim 4000$ and an ER of ~ 27 dB. The FSR is ~ 4.7 nm, which is consistent with the calculated four-bounce ray orbits FSR of ~ 4.9 nm.

We also characterize the silicon waveguide-coupled hexagonal microresonators. Fig. 12(d) shows the measured TE-polarized throughput spectrum of the fabricated device. Inset shows the top-view SEM of a fabricated 50-μm silicon round-cornered hexagonal microresonator filter with $R/L = 0.1$. The fabricated w is $\sim 0.35\ \mu$m, and g is $\sim 0.35\ \mu$m. Compared with square and octagonal microresonators, the spectrum exhibits a much lower Q of ~ 1500 and ER of ~ 15 dB, but is still nearly single mode. The FSR is ~ 4.2 nm, which is consistent with the calculated six-bounce ray orbits FSR of ~ 4.7 nm. We attribute the lower Q to the open-loop six-bounce mode in the hexagonal microresonators with $w \sim 0.35\ \mu$m. We note that in order to couple to a k-vector angle of $\sim 60°$, the waveguide width w should be $\sim 0.4\ \mu$m.

We remark that the square and hexagonal microresonators have their own issues to be addressed. For square microresonators, our previous numerical papers [20] and other similar papers in the literature [17], [22] suggest that small-sized square microresonators tend to support standing-wave modes due to the open-loop ray orbits being backward reflected after circulating a number of round trips. In order to mitigate the standing-wave resonances issues, our previous numerical paper suggested corner-cut designs for enabling traveling-wave resonances in square microresonators [21].
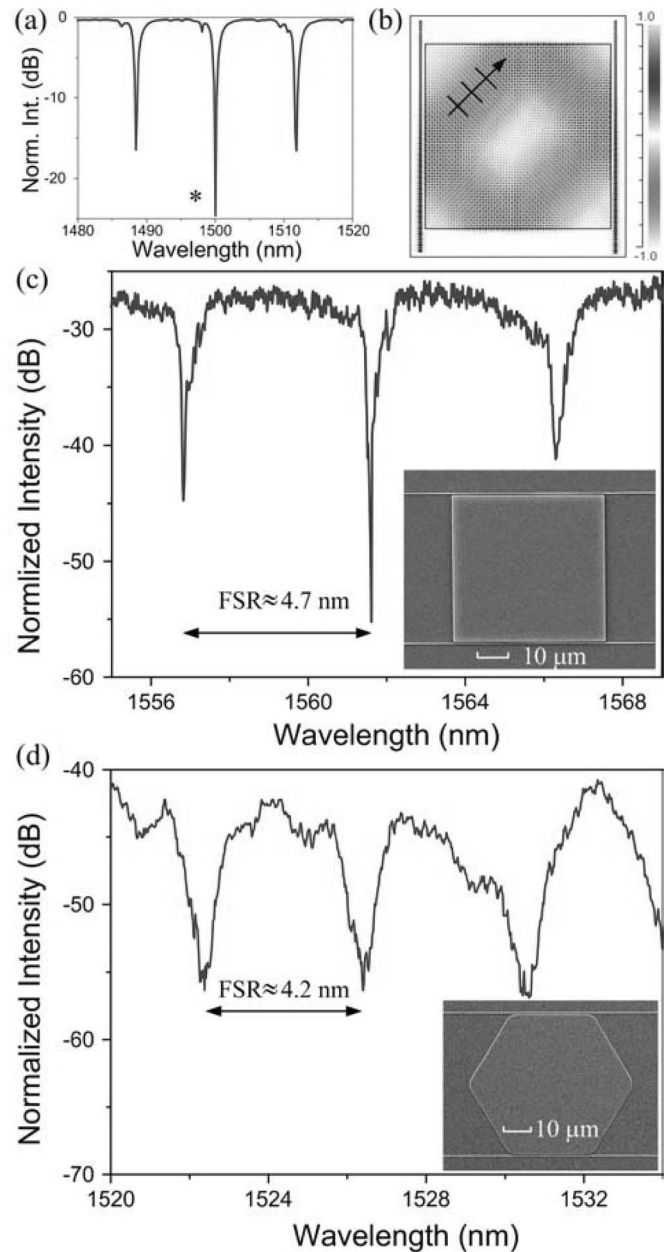

Fig. 12. (a) FDTD-simulated throughput-port spectrum (TE polarization) of a 25-μm waveguide-coupled square microresonator filter. (b) Simulated steady-state H-field pattern at resonance "*." (c) Measured TE-polarized throughput spectrum of the 50-μm silicon square microdisk. The top-view SEM of the square microresonator filter is shown (*inset*). (d) Measured TE-polarized throughput spectrum of the silicon waveguide-coupled 50-μm round-cornered hexagonal microresonator filter with $R/L = 0.1$. The top-view SEM of the filter is shown (*inset*).

For hexagonal microcavities with parallel waveguides coupling, the input- and output-coupled open-orbit ray angles are generally not the same (except for $\theta = 60°$) due to the odd number of bounces between the input and the output coupling to the parallel sidewalls. This means that in order to have symmetric input and output coupling with hexagonal microcavity, either the waveguides need to be coupled to alternate sidewalls, or the input- and output-coupled parallel waveguides need to have a slightly different width.

TABLE I
SILICON MICRORING, RACETRACK MICRORING, AND CIRCULAR MICRODISK DEVICES REPORTED IN THE LITERATURE
AND OUR POLYGONAL MICRORESONATOR DEVICES

Year	Author	Index contrast	D[†] (µm)	W[†] (µm)	G[†] (µm)	Modes	FSR (nm)	Q	ER[†] (dB)
Ring									
Oct., 2004	T. Baehr-Jones, *et al* [4]	air - Si	60	0.5	0.33	single	--	57,000	15.5
Dec., 2004	J. Niehusmann, *et al* [5]	air - Si	40	0.5	0.25	single	--	139,000	15
May, 2005	Q. Xu, *et al* [14]	Silica-Si	12	0.45	0.2	single	15	39,350	15
Racetrack									
July, 2003	A. Vörckel, *et al* [6]	air - Si	6 (1*)	0.4	0.16/ 0.2	single	24	2,580	12.8
May, 2004	P. Dumon, *et al* [7]	air - Si	10 (3*)	0.45	0.23	single	14	3,000	20
Sep., 2004	W. R. Headley, *et al* [8]	air - Si	800 (500*)	0.87	0.65	single	0.192	90,000	11.7
Mar., 2005	I. Kiyat, *et al* [9]	Silica-Si	700 (32*)	1	0.8	single	0.29	119,000	10.4
Oct., 2005	I. Kiyat, *et al* [10]	Silica-Si	120 (36*)	1	0.7	single	3	28,000	7
Disk									
July, 2005	A. Kazmierczak, *et al* [11]	air - Si	4	0.245	0.2	multi	50	2,000	20
Aug., 2005	T. Indukuri, *et al* [13]	Silica-Si	40	2	0.1	single	5	2,000	20
Polygon (our work)									
	Octagon	air - Si	50** (20.7*)	0.34	0.36	multi	4.7	10,000	15
	Hexagon	air - Si	50** (28.9*)	0.35	0.35	multi	4.2	1,500	15
	Square	air - Si	50** (50.0*)	0.3	0.45	multi	4.8	4,000	27

[†] **D: Diameter; W: waveguide width; G: gap separation; ER: Extinction ratio**

* **coupling length (µm)**

** **Sidewall-to-sidewall length (µm)**

It is of the essence to employ a round-cornered polygonal microresonator shape in order to obtain high-Q resonances. Our paper showed that round-cornered octagonal microresonators with a relatively large corner radius ($R/L = 0.3$) display resonance Q values less but close to (within a factor of three) those of a circular microresonator of same size. However, we caution that a large R/L ratio also means a short sidewall length. Our studies suggested that optimum R/L ratio for octagonal microresonators lies between ~ 0.3 and ~ 0.4 for L of 30–50 µm.

Another major design issue is the effect of the microresonator size and shape on the coupled **k**-vector directionality. The coupled **k**-vector directionality can be enhanced by lengthening the flat sidewall length, and thus favoring preferential coupling to only few modes. Our simulations of 30-µm microresonators revealed two major modes for octagonal microresonators, yet at least five modes for the circular microresonators. Our experiments on 50-µm microresonators revealed only two modes in octagonal microresonators, yet about eight modes in the circular microresonator.

The microresonator size and shape also affect the waveguide coupling efficiency. Our experiment on 50-µm octagonal microresonators suggested a $\kappa \sim 0.3$ for $R/L = 0.3$ with an air-

gap separation of ~ 0.36 µm. In contrast, our experiment on the 50-µm circular microresonator on the same chip suggested a $\kappa \sim 0.14$ with the same air-gap separation. A large κ suggests a relatively large tolerance to the air-gap spacing, and thus potentially eases the fabrication constraint.

In order to enable efficient coupling through a reasonable air-gap separation and sidewall interaction length, the silicon waveguide width should be chosen in the range of ~ 0.25–0.5 µm. For polygonal microresonators, it is thus practical to couple to four-bounce ray orbits in octagonal and square microresonators or six-bounce ray orbits in hexagonal microresonators.

Table I summarizes the key measured characteristics of silicon circular microring [4], [5], [14], racetrack microring [6]–[10], and circular microdisk devices [11], [13] reported in the literature, and of our silicon polygonal microresonator devices. Our fabricated air-gap separation of ~ 0.36 µm (with an etch depth of ~ 0.15 µm) between the submicrometer waveguides and the 50-µm microresonators significantly exceeds typical air-gap spacing reported in the literature for coupling to microring and microdisk resonators. Nonetheless, we demonstrated exceeding 10-dB ERs for octagonal microresonator filters and

other polygonal microresonator filters. However, because of the relatively large air-gap separations for both the input and output coupling, the drop-port intensity is below our detection limit.

Based on our paper, we believe that polygonal microresonator devices of various shapes and sizes deserve further theoretical and experimental research. We should seek to provide a direct experimental observation of the directional k-vector coupling along flat sidewalls, and experimentally demonstrate single-mode polygonal microresonator-based devices. Only then we could further exploit silicon polygonal microresonators for active switches and modulators applications using integrated p-i-n diodes [14], [33] and MOS capacitors [34].

ACKNOWLEDGMENT

REFERENCES

[1] B. E. Little, J. S. Foresi, G. Steinmeyer, E. R. Thoen, S. T. Chu, H. A. Haus, E. P. Ippen, L. C. Kimerling, and W. Greene, "Ultra-compact Si-SiO$_2$ microring resonator optical channel dropping filters," *IEEE Photon. Technol. Lett.*, vol. 10, no. 4, pp. 549–551, Apr. 1998.

[2] D. J. W. Klunder, F. S. Tan, T. van der Veen, H. F. Bulthuis, G. Sengo, B. Docter, H. J. W. M. Hoekstra, and A. Driessen, "Experimental and numerical study of SiON microresonators with air and polymer cladding," *J. Lightw. Technol.*, vol. 21, no. 4, pp. 1099–1110, Apr. 2003.

[3] T. Barwicz, M. A. Popović, P. T. Rakich, M. R. Watts, H. A. Haus, E. P. Ippen, and H. I. Smith, "Microring-resonator-based add-drop filters in SiN: Fabrication and analysis," *Opt. Express*, vol. 12, pp. 1437–1442, Apr. 2004.

[4] T. Baehr Jones, M. Hochberg, C. Walker, and A. Scherer, "High-Q ring resonators in thin silicon-on-insulator," *Appl. Phys. Lett.*, vol. 85, pp. 3346–3347, Oct. 2004.

[5] J. Niehusmann, A. Vörckel, P. H. Bolivar, T. Wahlbrink, W. Henschel, and H. Kurz, "Ultrahigh-quality-factor silicon-on-insulator microring resonator," *Opt. Lett.*, vol. 29, pp. 2861–2863, Dec. 2004.

[6] A. Vörckel, M. Mönster, W. Henschel, P. H. Bolivar, and H. Kurz, "Asymmetrically coupled silicon-on-insulator microring resonators for compact add-drop multiplexers," *IEEE Photon. Technol. Lett.*, vol. 15, no. 7, pp. 921–923, Jul. 2003.

[7] P. Dumon, W. Bogaerts, V. Wiaux, J. Wouters, S. Beckx, J. Van Campenhout, D. Taillaert, B. Luyssaert, P. Bienstman, D. Van Thourhout, and R. Baets, "Low-loss SOI photonic wires and ring resonators fabricated with deep UV lithography," *IEEE Photon. Technol. Lett.*, vol. 16, no. 5, pp. 1328–1330, May 2004.

[8] W. R. Headley, G. T. Reed, S. Howe, A. Liu, and M. Paniccia, "Polarization-independent optical racetrack resonators using rib waveguides on silicon-on-insulator," *Appl. Phys. Lett.*, vol. 85, pp. 5523–5525, Dec. 2004.

[9] I. Kiyat, A. Aydinli, and N. Dagli, "High-Q silicon-on-insulator optical rib waveguide racetrack resonators," *Opt. Express*, vol. 13, pp. 1900–1905, Mar. 2005.

[10] ——, "Polarization characteristics of compact SOI rib waveguide racetrack resonators," *IEEE Photon. Technol. Lett.*, vol. 17, no. 10, pp. 2098–2100, Oct. 2005.

[11] A. Kazmierczak, M. Brière, E. Drouard, P. Bontoux, P. Rojo-Romeo, I. O Connor, X. Letartre, F. Gaffiot, R. Orobtchouk, and T. Benyattou, "Design, simulation, and characterization of a passive optical add-drop filter in silicon-on-insulator technology," *IEEE Photon. Technol. Lett.*, vol. 17, no. 7, pp. 1447–1449, Jul. 2005.

[12] M. Borselli, T. J. Johnson, and O. Painter, "Beyond the Rayleigh scattering limit in high-Q silicon microdisks: Theory and experiment," *Opt. Express*, vol. 13, pp. 1515–1530, Mar. 2005.

[13] T. Indukuri, P. Koonath, and B. Jalali, "Subterranean silicon photonics: Demonstration of buried waveguide-coupled microresonators," *Appl. Phys. Lett.*, vol. 87, p. 081114, Aug. 2005.

[14] Q. Xu, B. Schmidt, S. Pradhan, and M. Lipson, "Micrometre-scale silicon electro-optic modulator," *Nature*, vol. 435, pp. 325–327, May 2005.

[15] M.-C. M. Lee and M. C. Wu, "MEMS-actuated microdisk resonators with variable power coupling ratios," *IEEE Photon. Technol. Lett.*, vol. 17, no. 5, pp. 1034–1036, May 2005.

[16] G. N. Nielson, D. Seneviratne, F. Lopez Royo, P. T. Rakich, Y. Avrahami, M. R. Watts, H. A. Haus, H. L. Tuller, and G. Barbastathis, "Integrated wavelength-selective optical MEMS switching using ring resonator filters," *IEEE Photon. Technol. Lett.*, vol. 17, no. 6, pp. 1190–1192, Jun. 2005.

[17] C. Manolatou and H. A. Haus, *Passive Components for Dense Optical Integration*. Norwell, MA: Kluwer, 2002.

[18] A. W. Poon, F. Courvoisier, and R. K. Chang, "Multimode resonances in square-shaped optical microcavities," *Opt. Lett.*, vol. 26, pp. 632–634, May 2001.

[19] Y. L. Pan and R. K. Chang, "Highly efficient prism coupling to whispering gallery modes of a square μ-cavity," *Appl. Phys. Lett.*, vol. 82, pp. 487–489, Jan. 2003.

[20] C. Y. Fong and A. W. Poon, "Mode field patterns and preferential mode coupling in planar waveguide-coupled square microcavities," *Opt. Express*, vol. 11, pp. 2897–2904, Nov. 2003.

[21] C. Y. Fong and A. W. Poon, "Planar corner-cut square microcavities: Ray optics and FDTD analysis," *Opt. Express*, vol. 12, pp. 4864–4874, Oct. 2004.

[22] ——, "Corner-cut square microcavity coupled waveguide crossing," in *Proc. Conf. Lasers Electro-Opt.*, San Francisco, CA, May 2004, vol. 2, p. 3.

[23] W. H. Guo, Y. Z. Huang, Q. Y. Lu, and L. J. Yu, "Mode quality factor based on far-field emission for square resonators," *IEEE Photon. Technol. Lett.*, vol. 16, no. 5, pp. 479–481, Feb. 2004.

[24] J. Wiersig, "Hexagonal dielectric resonators and microcrystal lasers," *Phys. Rev. A, Gen. Phys.*, vol. 67, p. 023807, Feb. 2003.

[25] N. Ma, F. K. L. Tung, S. F. Lui, and A. W. Poon, "Hexagonal micropillar cavities: Multimode resonances and open-loop resonance linewidth broadening," in *Proc. SPIE*, vol. 4986, pp. 153–160, Jan. 2003.

[26] N. Ma, C. Li, and A. W. Poon, "Laterally coupled hexagonal micropillar resonator add-drop filters in silicon nitride," *IEEE Photon. Technol. Lett.*, vol. 16, no. 11, pp. 2487–2489, Nov. 2004.

[27] C. Li, N. Ma, and A. W. Poon, "Waveguide-coupled octagonal microdisk channel add-drop filters," *Opt. Lett.*, vol. 29, pp. 471–473, Mar. 2004.

[28] C. Li and A. W. Poon, "Experimental demonstration of waveguide-coupled round-cornered octagonal microresonators in silicon nitride," *Opt. Lett.*, vol. 30, pp. 546–548, Mar. 2005.

[29] FullWAVE, Rsoft Inc., Research Software. [Online]. Available: http://www.rsoftinc.com

[30] S. Zheng, N. Ma, and A. W. Poon, "Experimental demonstration of waveguide-coupled hexagonal micropillar resonators with round-corners in silicon nitride," in *Proc. Conf. Lasers Electro-Opt.*, Baltimore, MD, May 2005, vol. 1, pp. 443–445.

[31] A. Yariv, "Universal relations for coupling of optical power between microresonators and dielectric waveguides," *Electron. Lett.*, vol. 36, pp. 321–322, Feb. 2000.

[32] UNIBOND SOI wafers, Soitec Inc. [Online]. Abailable: http://www.soitec.com

[33] L. Zhou and A. W. Poon, "Silicon-on-insulator electro-optically tunable waveguide-coupled microdisk resonators with selectively integrated p-i-n diodes," in *Proc. IEEE/LEOS 2nd Int. Conf. Group IV Photon.*, Antwerp, Belgium, Sep. 2005, pp. 23–25.

[34] C. Li and A. W. Poon, "Experimental demonstration and proposal of silicon-on-insulator octagonal microresonator devices," in *Proc. IEEE/LEOS 2nd Int. Conf. Group IV Photon.*, Antwerp, Belgium, Sep. 2005, pp. 162–164.

Chao Li received the B.S. and M.S. degrees in physics from Tsinghua University, Beijing, China, in 1998 and 2001, respectively. He is currently working toward the Ph.D. degree in electronic and computer engineering at The Hong Kong University of Science and Technology, Hong Kong.

Linjie Zhou received the B.S. degree in microelectronics from Peking University, Beijing, China, in 2003. He is currently working toward the Ph.D. degree in electronic and computer engineering at The Hong Kong University of Science and Technology, Hong Kong.
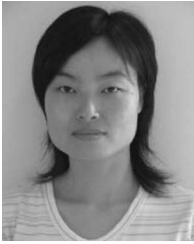
Shengmei Zheng received the B.S. degree in optical engineering from Zhejiang University, Zhejiang, China, and the Master's degree in electrical and electronic engineering from The Hong Kong University of Science and Technology, Hong Kong, in 2003 and 2006, respectively.

She is currently with The Hong Kong Applied Science and Technology Research Institute Company Ltd., Hong Kong. Her current research interests include integrated optical devices, including microresonator-coupled parallel waveguides/waveguide crossings for channel add-drop filters and routers in optical communications, and blue LED radiation pattern modification, current spreading improvement, and extraction efficiency enhancement.

Andrew W. Poon (M'01–A'02) received the B.A. (Hons.) degree from the University of Chicago, Chicago, IL, and the M.Phil. and Ph.D. degrees from Yale University, New Haven, CT, in 1995, 1998, and 2001, respectively, all in physics.

He is currently an Assistant Professor in the Department of Electronic and Computer Engineering, The Hong Kong University of Science and Technology, Hong Kong. His current research interests include experiments and designs of novel optical microresonators, and silicon-based photonic passive and active devices and circuits.